

AD-A245 816

MTL TR 91-50



AD

2

# COMPARISON OF CERAMIC UNIAXIAL COMPRESSION SPECIMENS THROUGH DETAILED FINITE ELEMENT MODELLING

PAUL V. CAVALLARO

MECHANICS AND STRUCTURES BRANCH

December 1991



Approved for public release; distribution unlimited.

92 2 1 145



US ARMY  
LABORATORY COMMAND  
MATERIALS TECHNOLOGY LABORATORY

92-03313



U.S. ARMY MATERIALS TECHNOLOGY LABORATORY  
Watertown, Massachusetts 02172-0001

The findings in this report are not to be construed as an official Department of the Army position, unless so designated by other authorized documents.

Mention of any trade names or manufacturers in this report shall not be construed as advertising nor as an official indorsement or approval of such products or companies by the United States Government.

#### DISPOSITION INSTRUCTIONS

Destroy this report when it is no longer needed.  
Do not return it to the originator.

SECURITY CLASSIFICATION OF THIS PAGE (When Data Entered)

DD FORM 1 JAN 73 1473

EDITION OF 1 NOV 65 IS OBSOLETE

UNCLASSIFIED

SECURITY CLASSIFICATION OF THIS PAGE (When Data Entered)

Block No. 20

#### ABSTRACT

Mechanical properties of advanced structural materials are determined through physical testing. In the area of high strength ceramics, routine testing includes techniques for measuring compressive strength. Successful and efficient characterization of compressive strength and other properties allows the design engineer to exploit the maximum structural potential for these advanced materials. This report details comparisons made between two proposed dumbbell-shaped, uniaxial ceramic compression specimens. Comparisons were made for alumina ( $\text{Al}_2\text{O}_3$ ) material through detailed finite element modeling. Differences in stress distributions resulting from both geometries were then applied to experimentally obtained strength values to determine if these values were representative of the same statistical population.

# SYMBOLS

$\delta_z$  . . . . . Uniform displacement boundary condition  
 $E$  . . . . . Modulus of elasticity  
 $\nu_{rz}$  . . . . . Poisson's ratio  
 $SCF$  . . . . . Axial stress concentration factor  
 $\sigma_c$  . . . . . Compressive strength of material  
 $\sigma_{rr}$  . . . . . Radial stress component  
 $\sigma_{zz}|g$  . . . . . Axial gage section stress  
 $\sigma_{xx}|g,avg$  . . . . . Average axial gage section stress  
 $\sigma_{zz}|f$  . . . . . Axial stress at transition fillet #1  
 $\sigma_{\theta\theta}$  . . . . . Hoop stress component  
 $\sigma_1$  . . . . . First principal stress  
 $\sigma_3$  . . . . . Third principal stress  
 $\sigma_3|g,avg$  . . . . . Average gage section third principal stress  
 $\tau_{rz}$  . . . . . Shear stress component  
 $\tau_{rz}|g,avg$  . . . . . Average gage section shear stress  
 $\tau_{rz}|g,max$  . . . . . Maximum gage section shear stress  
 $u_r$  . . . . . Radial displacement component  
 $u_z$  . . . . . Longitudinal displacement component

Accession For	
NTIS GRA&I	<input checked="" type="checkbox"/>
DTIC TAB	<input type="checkbox"/>
Unannounced	<input type="checkbox"/>
Justification	
By	
Distribution	
Availability Codes	
Avail and/or	
Dist	Special
A-1	

## CONTENTS

	Page
INTRODUCTION . . . . .	1
DESCRIPTION OF THE TEST SETUP . . . . .	1
FINITE ELEMENT ANALYSIS . . . . .	2
Coarse Density B-Type Model . . . . .	2
Fine Density B-Type Model . . . . .	4
Fine Density A-Type Model . . . . .	4
SUMMARY OF RESULTS . . . . .	5
RECOMMENDATIONS . . . . .	8
ACKNOWLEDGMENTS . . . . .	8

## INTRODUCTION

A critical requirement in the design of uniaxial compression specimens is that failure be reproducible at a controlled location; i.e., gage section, upon exceeding the ultimate material strength. Failures originating elsewhere may not be indicative of a uniaxial state of stress and, therefore, may not accurately reflect the ultimate compressive strength of the material.

Rapid fracture rates are commonly associated with compression testing of high strength ceramics. These fracture rates prevent the origin of failure initiation from being determined by conventional methods. Compression tests performed using recommended loading rates<sup>1</sup> (45 KN/min, 10,000 lb/min) result in instantaneous failures at ultimate load. Therefore, performance comparisons made between various specimen configurations were based upon statistical evaluations of test data and visual inspection of failed sections. Strength data containing mixed failure modes yielded conservative ultimate compressive strengths and increased scatter of data.

The need for an optimized compression test for high strength (<1 GPa) ceramics resulted in the development of the two specimen geometries shown in Figure 1. Tracy<sup>2</sup> developed and successfully used the A-type specimen for compression testing of 94% alumina ( $\text{Al}_2\text{O}_3$ ). The B-type specimen was a modified version of the latter and was developed by Dunlay et al.<sup>3</sup> Actual dimensions for each are shown in Table 1. The specimen shapes were of the familiar dumbbell type and their relative differences were due to variations in proportionality only; i.e., gage section lengths and diameters. Both specimens were designed to: (1) provide uniaxial stress distributions within their respective gage area, (2) ensure fracture within the gage areas, (3) minimize effects of local stress risers, and (4) provide the optimum gage length for column buckling stability.

Table 1. SPECIMEN DIMENSIONS

Specimen Type	Overall Length [cm (in.)]	Gage Length [cm (in.)]	Gage Diameter [cm (in.)]	Gage Volume [cm <sup>3</sup> (in. <sup>3</sup> )]	End Cap Diameter [cm (in.)]
A	3.650 (1.44)	0.953 (0.375)	0.635 (0.25)	0.302 (0.018)	1.270 (0.5)
B	3.050 (1.20)	0.762 (0.30)	0.508 (0.20)	0.154 (0.009)	1.020 (0.40)

The scope of this effort was twofold. First, to analytically obtain and compare stress distributions and effects of stress concentrations for both the A-type and B-type uniaxial compression specimens. Secondly, to determine if the compressive strengths measured with the A-type and B-type specimens were from the same statistical population and independent of specimen volume.

## DESCRIPTION OF THE TEST SETUP

Ceramic dumbbell-shaped specimens were loaded using a universal test machine with precision machined steel fixtures. The specimen ends, called end caps, were designed as such to minimize eccentricities due to bending. Tungsten carbide (WC) loading blocks were positioned on

1. ASTM Standard Test Method for Compressive (Crushing) Strength of Fired Whiteware Materials (ASTM C 773). American Society for Testing and Materials, Philadelphia, PA, 1983.
2. TRACY, C. A. *A Compression Test for High Strength Ceramics*. Journal of Testing and Evaluation, v. 15, no. 1, January 1987, p. 14-19.
3. DUNLAY, W. A., et al. *A Proposed Uniaxial Compression Test for High Strength Ceramics*. U. S. Army Materials Technology Laboratory, TR 89-89.

both specimen end caps and were used to ensure that fracture did not initiate within the end caps. Furthermore, since the compliancy for WC was less than that of  $\text{Al}_2\text{O}_3$ , the differential shear stress along the interface provided a degree of lateral motion restraint to the end caps. This restraining effect assisted in maintaining alignment of the components within the load path and preventing radial tensile failures within the specimen end caps. The geometry of the loading blocks are shown in Figure 2.

## FINITE ELEMENT ANALYSIS

In order to assess all, if any, structural deficiencies of the A-type and B-type ceramic compression specimens, it was necessary to perform a finite element analysis (FEA) on each. The models would efficiently verify: (1) the existence of a uniaxial compressive stress distribution in the gage section, (2) any stress concentrations present within each specimen, (3) location and magnitude of the maximum compressive stress, and (4) if any significant tensile stresses existed within the specimens, or more specifically, the end caps. Three models in particular were developed which included both coarse and fine density B-type specimen meshes and one fine density A-type specimen mesh. Contour plots of various stress components allowed visual inspection of the respective stress distributions.

### Coarse Density B-Type Model

Earlier experimental and finite element analysis efforts on the B-type specimen were performed by Dunlay et al.<sup>3</sup> on a wide variety of high strength ceramic materials. Results of linear-elastic finite element solutions were presented for each material.

The current effort began with a regeneration of the same B-type specimen model developed in Reference 3. This was performed to ensure repeatability of previous analysis results. The specimen portion of the model consisted of 410 eight noded, isoparametric, quadrilateral elements employing quadratic displacement functions. Since the specimen shape and applied boundary conditions were axisymmetric, a two-dimensional quarter model configuration was used, as shown in Figure 3. Nodal displacement constraints along the left and lower boundaries reflected the axisymmetric nature of the specimen geometry.

Only the  $\text{Al}_2\text{O}_3$  materials was considered in this effort since compression test data for this material existed for both A and B specimen types. The material properties for the  $\text{Al}_2\text{O}_3$  specimens and WC loading blocks used in the FEA modelling were taken from Reference 3 and are shown in Table 2.

Table 2. MATERIAL PROPERTIES

Material	$\sigma_c^*$ (GPa)	$E^\circ$ (GPa)	$\nu^\circ$
$\text{Al}_2\text{O}_3$ A-Type	3.49	280	0.23
$\text{Al}_2\text{O}_3$ B-Type	3.59	280	0.23
WC <sup>∞</sup>	4.29	606	0.28

\* Uniaxial compressive strength

° Elastic modulus sonic (strain gage) method

° Poisson's ratio sonic method

∞ Kennametal (TM) grade K3406

' Coors Ceramic Co., AD94



As recommended in Reference 3, the loading conditions imposed on the FEA model should be such that the axial compressive stress within the gage section ( $\sigma_{zz|g}$ ) approximated the compressive strength ( $\sigma_c$ ) of the  $\text{Al}_2\text{O}_3$  material. Corresponding, experimentally obtained compressive strengths ( $\sigma_{zz|g}$ ) for the A-type and B-type specimens were 3.49 GPa and 3.59 GPa, respectively.<sup>3</sup>

The coarse B-type specimen model was loaded by imposing a uniform, vertical displacement condition ( $\delta_z$ ) across the top surface of the loading block. An assumption of infinite friction was made along the interface between the specimen and loading block. Work performed in Reference 1 validated the assumption of infinite friction and its effects on model accuracy.

The displacement used to satisfy the gage section stress approximation was  $6.2 \times 10^{-3}$  meters in the negative Z (vertical) direction,  $\delta_z$ . Figure 3 shows the deformed B-type specimen mesh. This resulted in the gage section average axial stress  $\sigma_{zz|g,avg}$  of -3.677 GPa. A plot of the axial stress distribution is shown in Figure 4a. Radial ( $\sigma_{rr}$ ) and hoop ( $\sigma_{\theta\theta}$ ) stresses were tensile in the gage section and were less than 1% of the axial stress. Plots of these components are shown in Figures 4b and 4c. Also in this region, the average compressive principal stress ( $\sigma_{3,avg} = -3.675$  GPa) was nearly identical to the average axial stress ( $\sigma_{zz|g,avg} = -3.677$  GPa) indicating that the shear stress ( $\tau_{rz|g,avg} = 4 \times 10^{-4}$  GPa) was practically zero. All averaged gage section results were based upon stresses sampled at the fifth Gaussian integration point within elements located along the boundary defined by  $Z = 0$ ,  $0 \leq r \leq r_0$ . See Figure 5 for locations of Gaussian integration points. The axial compressive stress  $\sigma_{zz}$  was essentially uniform along this boundary being only 0.5% greater at the center than the edge.

Primary attention was given to the transition point between the gage section and fillet #1. Referring back to Figure 3, bending was evident about this point. The axial stress at the point of transition  $\sigma_{zz|f}$  was -4.029 GPa. In comparison to the gage section average axial stress  $\sigma_{zz|g,avg}$  of -3.677 GPa, it was readily apparent that a local stress concentrator existed at this point. The related stress concentration factor (SCF) was defined as:

$$SCF = \frac{\sigma_{zz|f}}{\sigma_{zz|g,avg}} \quad (1)$$

and is valid for linearly elastic materials. (In this class of materials, the SCF is solely dependent upon the geometry and neither the applied stress nor the material properties.) The resulting SCF value for the coarse B-type specimen model was 1.096. As a result of this stress concentration, the transition point between the gage section and fillet #1 was likely to be the location of failure initiation within the specimen.

Radial  $\sigma_{rr}$  and hoop  $\sigma_{\theta\theta}$  stress components within the specimen end caps were tensile with maximum magnitudes of 127 MPa and 217 MPa, respectively. The maximum tensile radial stress was located along the axial centerline, as shown in Figure 4b. The maximum tensile hoop stress existed at fillet #2 and is shown in Figure 4c. Since the hoop stress is tensile and dominates within the specimen end cap, the first principal stress  $\sigma_1$  (maximum tensile) shares the same peak magnitude and location. Additional stress component contour plots are shown in Figures 4d through 4f.

### Fine Density B-Type Model

The refined B-type model of Figure 6 was generated for determining the effects of mesh density and convergence on the various stress components. The number of specimen elements used in this model was increased uniformly to 663 (253 more than that found in the original Dunlay and coarse B-type models). This resulted in a 30% increase in the number of elements located within the gage section. The axisymmetric boundary constraints, uniform displacement condition  $\delta_z$ , and material property sets used were identical to those of the coarse B-type model.

Results indicated that the mesh refinement effects were minimal. The most significant change was found within the end cap. A decrease in the maximum tensile radial stress  $\sigma_{rr}$  by 2.36% was realized. At the transition point between fillet #1 and the gage section, the axial stress  $\sigma_{zz}|_f$  decreased by 0.10%. The gage section average axial stress  $\sigma_{zz}|_{g,avg}$  also decreased but only by 0.08%. The SCF decreased slightly to 1.095. However, the transition point between fillet #1 and the gage section remained as the expected location of failure initiation within the specimen.

In the gage section, the average principal compressive stress ( $\sigma_3|_{g,avg} = -3.672$  GPa) varied from the average axial stress ( $\sigma_{zz}|_{g,avg} = -3.674$  GPa) by -0.04%. It follows, therefore, that the shear stress was essentially zero ( $\tau_{rz}|_{g,max} = 3 \times 10^{-4}$  GPa). A nearly uniaxial state of stress was shown to exist in the gage section along the line ( $z = 0, 0 \leq r \leq r_0$ ) with  $\sigma_{zz}|_g$  varying only 0.5% between the center and the edge.

All other stress components varied from those of the coarse B-type model by less than 0.5%. Locations of maxima/minima stress components and principal stresses were the same for the coarse B-type model. The deformed model and stress contours are shown in Figure 6, and Figures 7a through 7f, respectively.

### Fine Density A-Type Model

A finite element model of the A-type specimen was produced with the same number of elements used in the refined B-type mesh, as shown in Figure 8. The axisymmetric boundary constraints and material property sets matched those of the previously described models.

Experimental data of the  $Al_2O_3$  material was available for the A-type specimen. The obtained compressive strength was -3.49 GPa.<sup>3</sup> To satisfy the gage section axial stress requirement, the loading condition must be such that  $\sigma_{zz}|_g$  approximated the compressive strength of the material. A uniform vertical displacement condition,  $\delta_z = -7.2 \times 10^{-3}$  meters, across the top surface of the loading block provided a nearly uniaxial state of stress within the gage section. The average gage section axial stress,  $\sigma_{zz}|_{g,avg}$ , and average compressive principal stress,  $\sigma_3|_{g,avg}$ , were -3.479 GPa and -3.475 GPa, respectively. Along the boundary ( $z = 0, 0 \leq r \leq r_0$ ), the axial stress  $\sigma_{zz}|_g$  was only 0.61% greater at the center than the edge. The maximum shear stress,  $\tau_{rz}$ , within this section was  $3 \times 10^{-4}$  GPa.

The maximum axial compressive stress occurred at the transition point between the gage section and fillet #1. This stress,  $\sigma_{zz}|_f$ , was -3.881 GPa and reflected the deformation by bending. Correspondingly, the SCF was 1.116. As results of the previous B-type

models indicated, the A-type specimen was also susceptible to failure initiation at this point of transition. Maximum radial and hoop stresses were tensile in the end cap with magnitudes of 139 MPa and 212 MPa, respectively. The deformed A-type model and associated stress contour plots are shown in Figure 8 and Figures 9a through 9f, respectively.

### SUMMARY OF RESULTS

Finite element modelling was successfully performed on the A-type and B-type ceramic uniaxial compression specimen designs. Stress components and stress concentration factors obtained for each model developed herein are tabulated in Tables 3 through 5. Comparisons made between the current effort and that reported by Dunlay et al. provided overall agreement for the B-type specimen. No comparisons were available for the A-type specimen since it was modelled only in the current effort.

Table 3. MAXIMUM COMPRESSIVE AND SHEAR STRESSES

Stress Component (GPa)	Finite Element Model				Max. Location (See Map*)
	Dunlay B-Type	Coarse B-Type $\delta_z = -0.0062$	Refined B-Type $\delta_z = -0.0062$	Fine A-Type $\delta_z = -0.0072$	
$\sigma_{zz} _{g,avg}$	-3.59	-3.677	-3.674	-3.479	—
$\sigma_{zz} _f$	-3.59	-4.029	-4.025	-3.881	A
$\sigma_{rr}$	N/A	-0.386	-0.387	-0.444	B
$\tau_{rz}$	N/A	-0.860	-0.859	-0.908	D
$\sigma_1$	N/A	-0.252	-0.252	-3.939	E
$\sigma_3$	-3.96	-4.038	-4.034	-3.895	A

\*See Table 5 for location map.

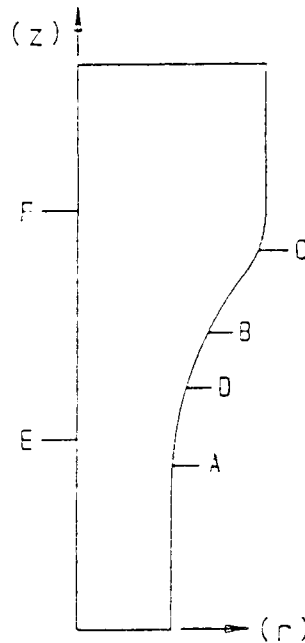
Table 4. STRESS CONCENTRATION VALUES  
AT TRANSITION POINT BETWEEN GAGE  
SECTION AND FILLET #1

Specimen Model	SCF
Dunlay B-Type	1.100
Coarse B-Type*	1.096
Refined B-Type*	1.095
Fine A-Type*	1.116

\*Based upon averaged gage section stress ( $\sigma_{zz}$ ) at Gaussian point #5 on line ( $z = 0, 0 \leq r \leq r_0$ ).

Table 5. MAXIMUM TENSILE STRESSES

Stress Component (GPa)	Finite Element Model				Max. Location (See Map)
	Dunlay B-Type	Coarse B-Type $\delta_z = -0.0062$	Refined B-Type $\delta_z = -0.0062$	Fine A-Type $\delta_z = -0.0072$	
$\sigma_{rr}$	0.126	0.127	0.121	0.139	F
$\sigma_{\theta\theta}$	0.213	0.217	0.216	0.212	C
$\sigma_1$	0.213	0.217	0.216	0.212	C



Maximum Stress Location Map

Correlation of the results between the Dunlay and coarse B-type specimen models was affected by the approximation imposed on the gage section axial stress. The constraint imposed on matching ultimate compressive strengths to gage section axial stresses was not practical since  $\sigma_{zz}|_g$  varied along the boundary ( $z = 0, 0 \leq r \leq r_0$ ) for each model. Results documented by Dunlay et al. did not provide such a match, specifically along the boundary ( $z = 0, 0 \leq r \leq r_0$ ). Hence, the current effort treated the constraint only as an approximation and determined the variability of stresses within the gage section more accurately.

Results of the A-type and B-type specimen models exhibited a uniaxial state of compressive stress within the gage sections. Negligible uniformity variations of the axial stress,  $\sigma_{zz}|_g$ , from the centers of the gage sections to the outer surfaces existed and were less than 0.61%. Furthermore, all models suggested that failure initiation would originate at the transition points between the gage sections and fillet #1. Local stress risers were determined at these transitions and the resulting SCFs were determined to be: 1.116 for the A-type, 1.096 for the coarse B-type specimen, and 1.095 for the refined B-type specimen. Consequently,

strength data acquired through either the A-type or B-type specimen configuration may not provide a true measure of a material's ultimate compressive strength. Such data should be treated as conservative approximations of ultimate compressive strength.

Experimental results obtained for the  $\text{Al}_2\text{O}_3$  material indicated that greater ultimate compressive strength was observed with the B-type specimen. Furthermore, to evaluate the issue of specimen volume dependency on ultimate strength, two paired statistic T-tests were performed. The first T-test was conducted on compression test data using the combined population of A-type and B-type specimens. The second T-test performed was based upon a corrected version of the same combined population. This correction consisted of multiplying the ultimate compression data for each specimen by its respective SCF to provide the maximum stress. Since the rapid fracture rates of high strength ceramics prevent the location of failure initiation from being detected by conventional means, it was assumed that all specimens failed at the fillet-gage transition. The original and corrected values for each specimen are listed in Table 6.

Table 6. UNIAXIAL COMPRESSIVE STRENGTH FOR  $\text{Al}_2\text{O}_3$

Test No.	Experimental Test Results* - Ultimate Stress (GPa)			
	A-Type Spec.	A-Type Spec. Corrected <sup>†</sup>	B-Type Spec.	B-Type Spec. Corrected*
1	3.51	3.92	3.56	3.90
2	3.42	3.82	3.59	3.93
3	3.40	3.79	3.68	4.03
4	3.43	3.83	3.80	4.16
5	3.45	3.85	3.56	3.90
6	3.56	3.97	3.60	3.95
7	3.61	4.03	3.61	3.96
8	3.49	3.89	3.44	3.77
9	3.44	3.84	3.41	3.74
10	3.63	4.05	3.70	4.06
Mean	3.49 ± 2%	3.90 ± 2%	3.59 ± 3%	3.94 ± 4%

\*See Reference 3 for uniaxial compression test data.

<sup>†</sup>Multiplied by respective stress concentration factor (SCF).

Results of the T-tests showed that the original data passed at only the 1% significance level while the corrected data passed at better than the 20% significance level. Thus, it is probable that the compressive strength of the ceramic material was independent of the specimen volume tested (unlike the tensile strength which decreases with increasing specimen volume and follows a Weibull distribution).

Stress concentration factors derived in the current effort promote the use of the B-type specimen for realization of greater, more accurate ultimate strengths. Furthermore, since the volume of and the load required to fracture the B-type specimen are substantially less than that of the A-type specimen, it is more economically and statistically desirable to manufacture the former.

## RECOMMENDATIONS

Continual development of uniaxial ceramic compression specimens is recommended to alleviate effects of local stress concentrations in the vicinity of surface transition points. Work performed by Oplinger et al.<sup>4</sup> suggests the use of a streamline-shaped profile for uniaxial tensile specimens of various materials. The streamline concept proves (1) surface boundaries for which potential stress risers are eliminated at transition points, (2) increased probability of gage section failures, and (3) reduction in scatter of test data. This approach warrants further consideration as an alternative for designing uniaxial ceramic compression specimens. An experimental testing effort is also recommended to confirm the volume independence on the compressive strengths of ceramics.

## ACKNOWLEDGMENTS

The author would like to express sincere appreciation to Mr. Michael Slavin of the Ceramics Research Branch for his continued support and informative discussions regarding the ceramic compression specimens and related statistics input.

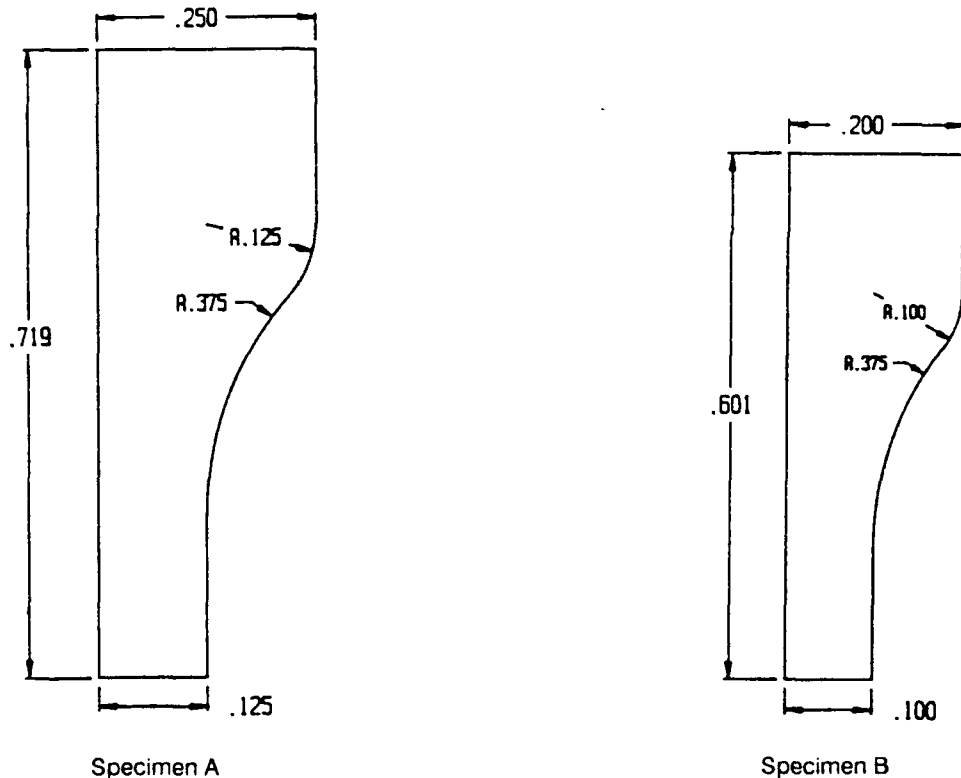
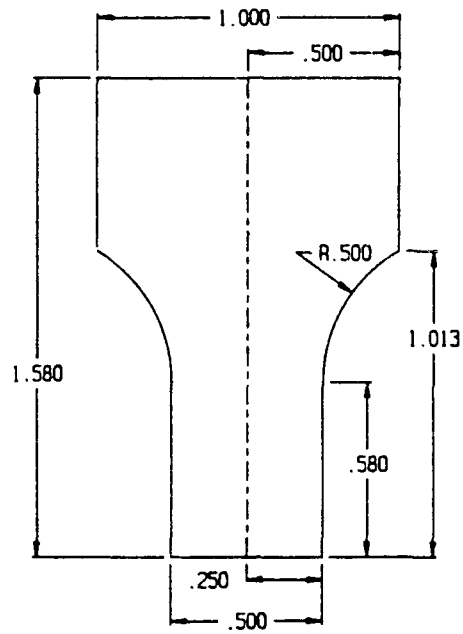
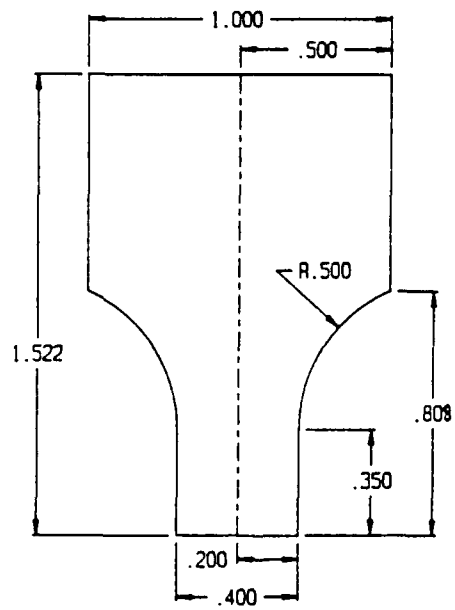


Figure 1. Specimen configurations (quarter geometries shown).

4. OPLINGER, D. W., et al. *On the Streamline Specimen for Tension Testing of Composite Materials*. American Society for Testing and Materials, Philadelphia, PA, 1985, p. 532-554.

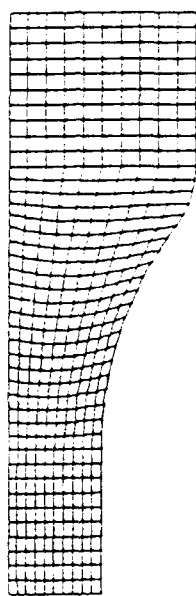
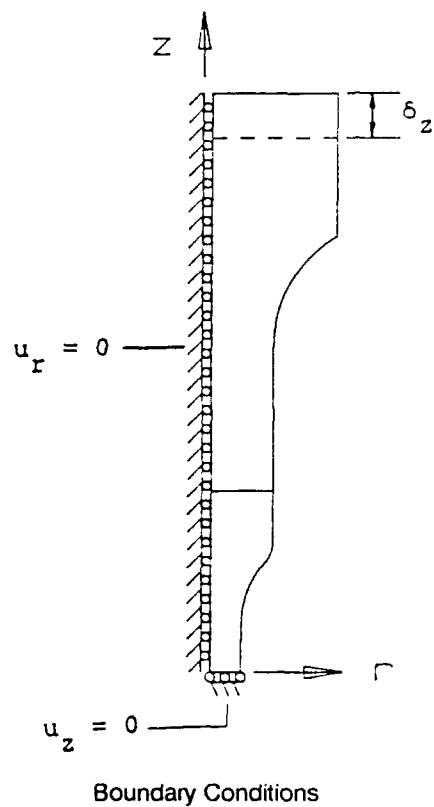
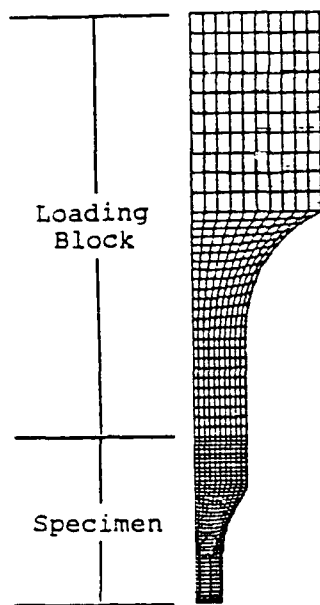


A-Specimen loading block

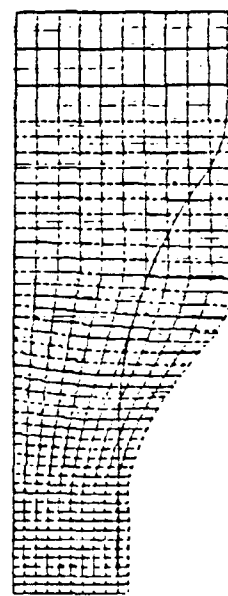


B-Specimen loading block

Figure 2. Loading block geometries.



Specimen



Deformed Model  
(Deformation is not to scale)

Figure 3. B-type coarse model.



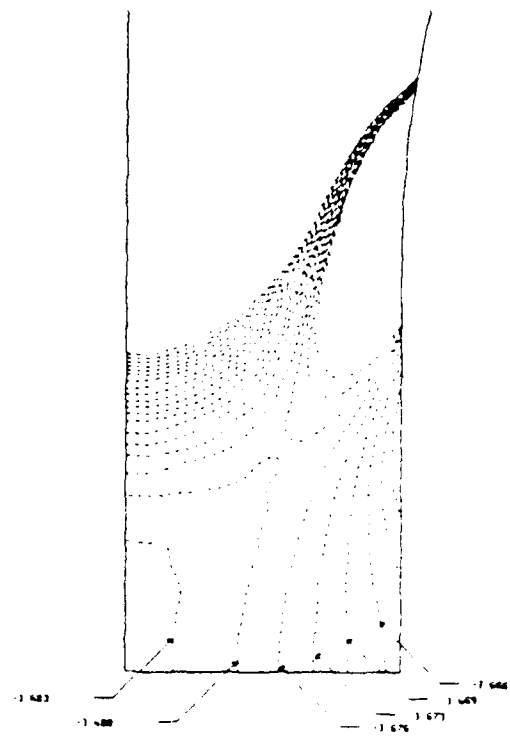
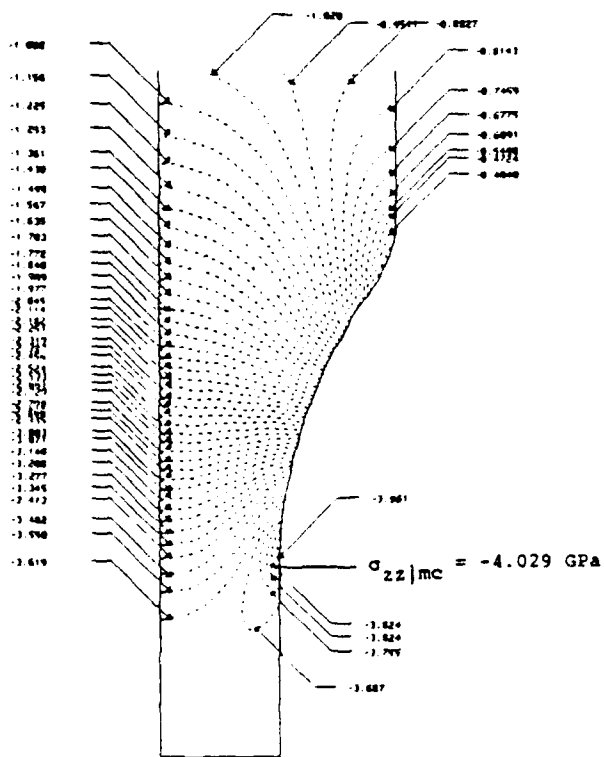


Figure 4a. Axial stress component ( $\sigma_{zz}$ ).

Gage Section Elargement

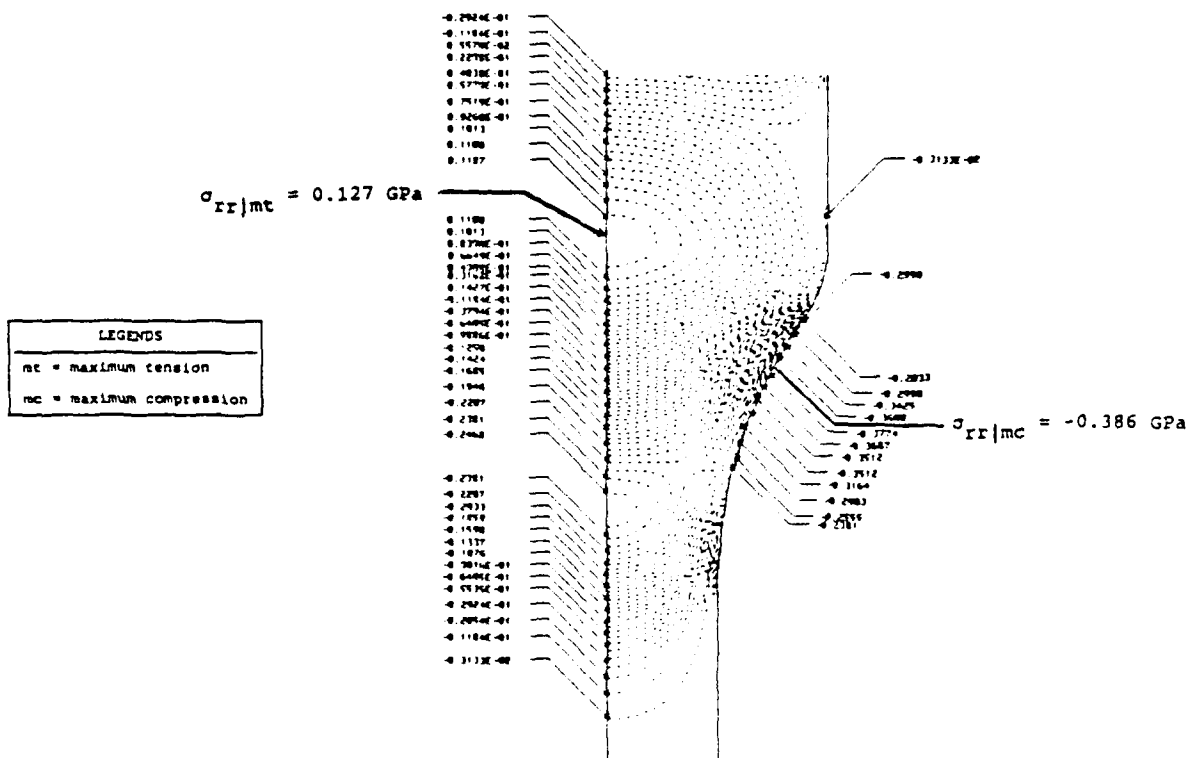
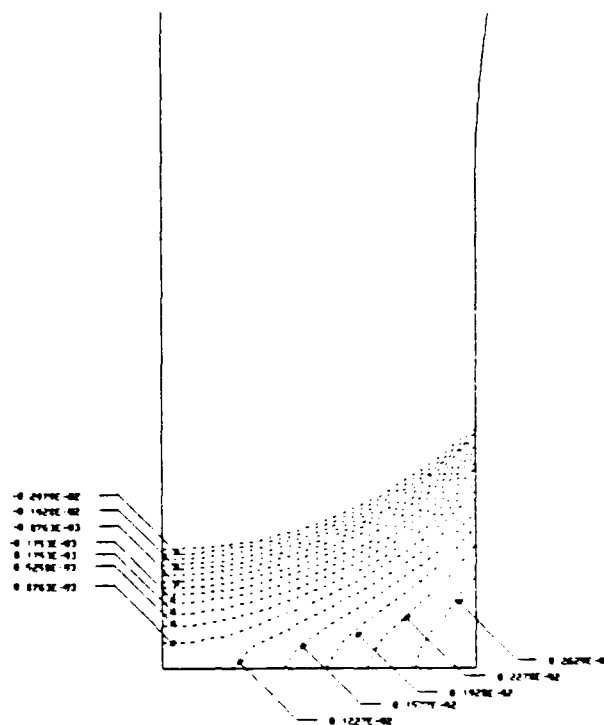
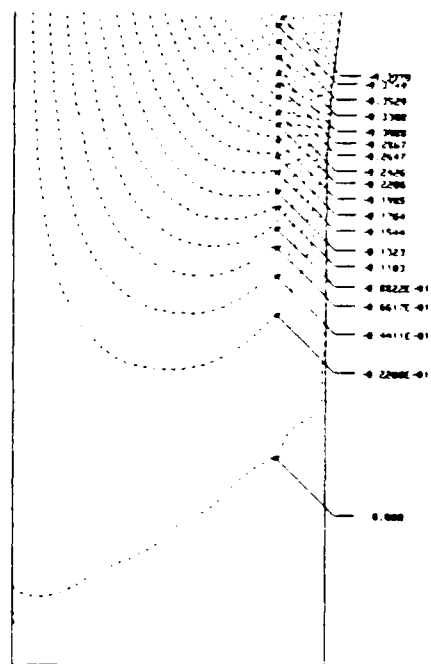


Figure 4b. Radial stress component ( $\sigma_{rr}$ ).



### Gage Section Enlargement



### Gage Section Enlargement

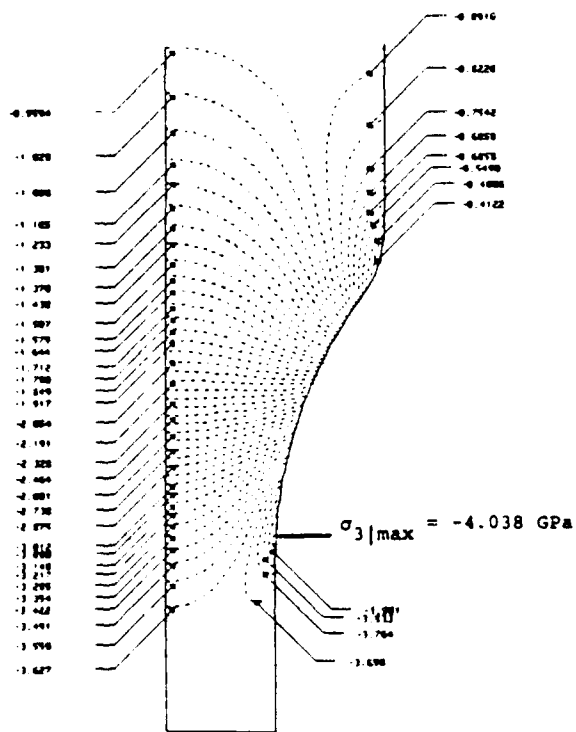
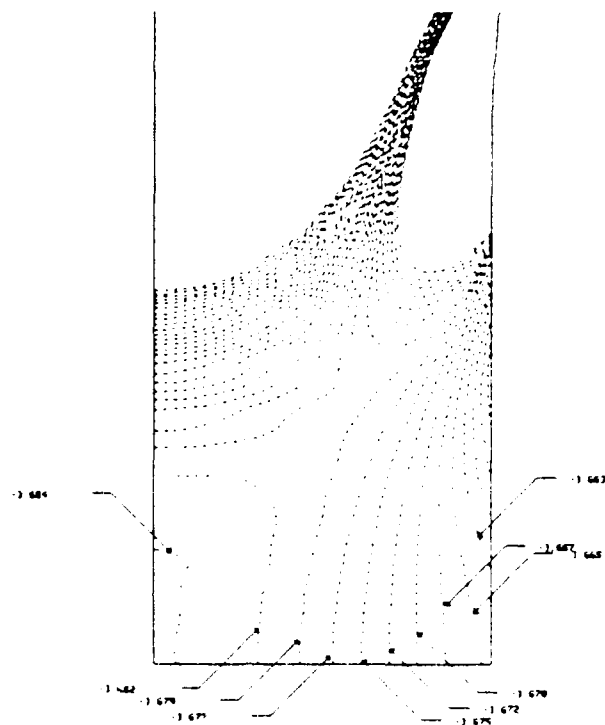


Figure 4e. 3rd principal stress ( $\sigma_3$ ).



Gage Section Enlargement

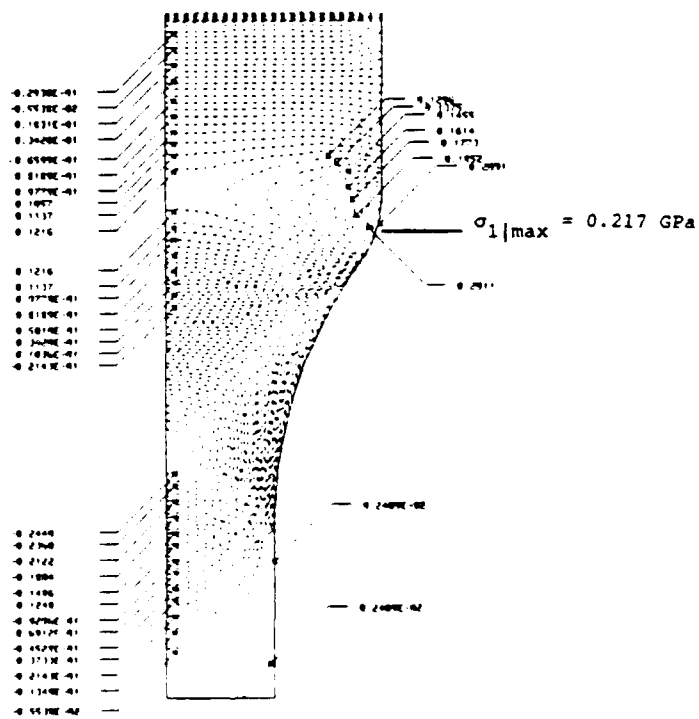


Figure 4f. 1st principal stress ( $\sigma_1$ ).

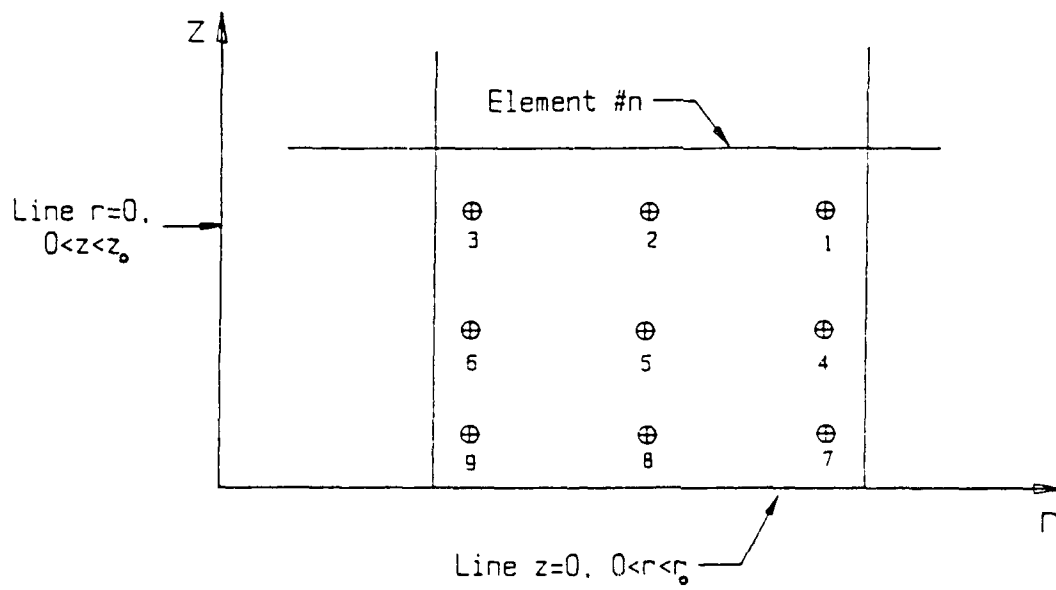
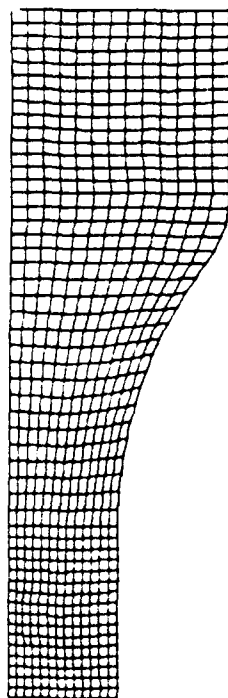


Figure 5. Gaussian integration points numbering scheme.

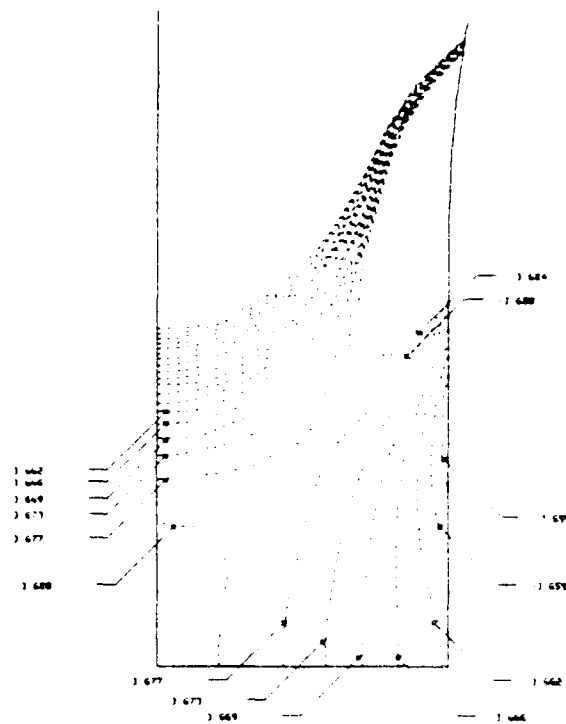


Specimen

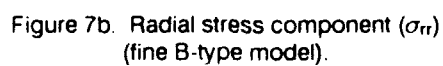
(Not Available)

Deformed Model  
(Deformation is not to scale)

Figure 6. B-type fine model.



### Gage Section Enlargement



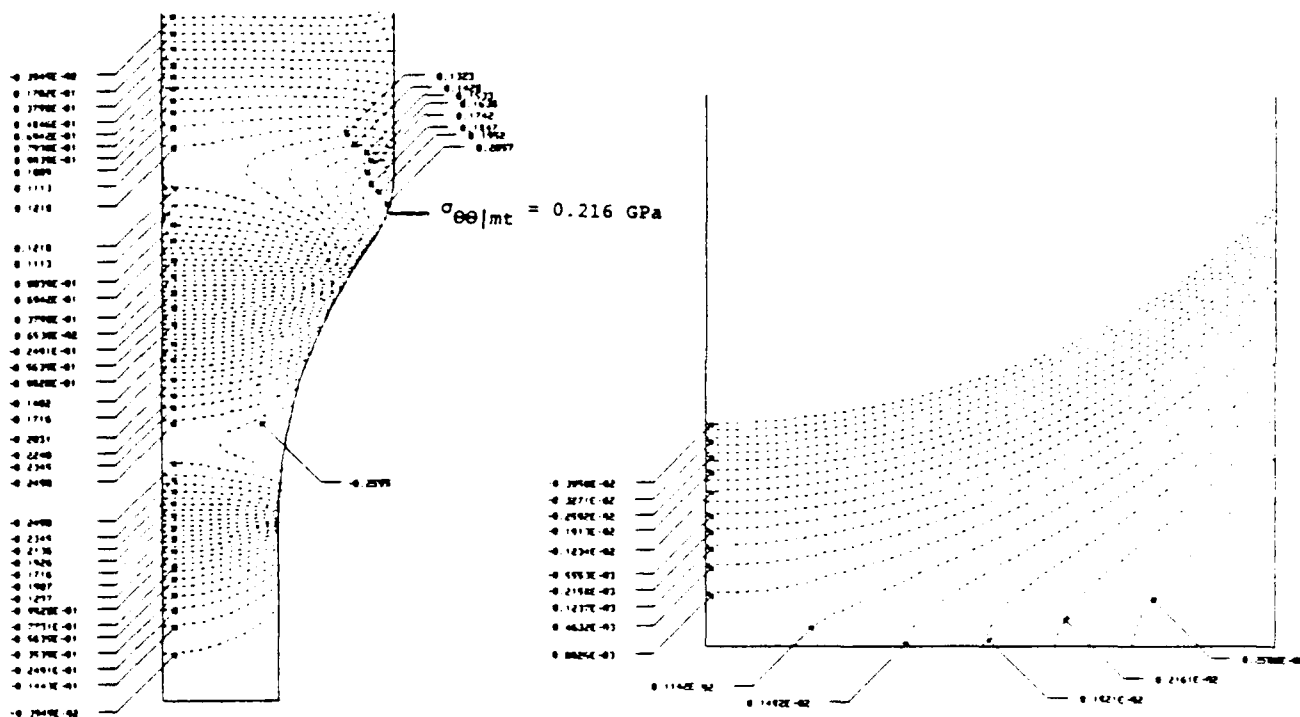


Figure 7c. Hoop stress component ( $\sigma_{\theta\theta}$ )  
(fine B-type model).

Gage Section Enlargement

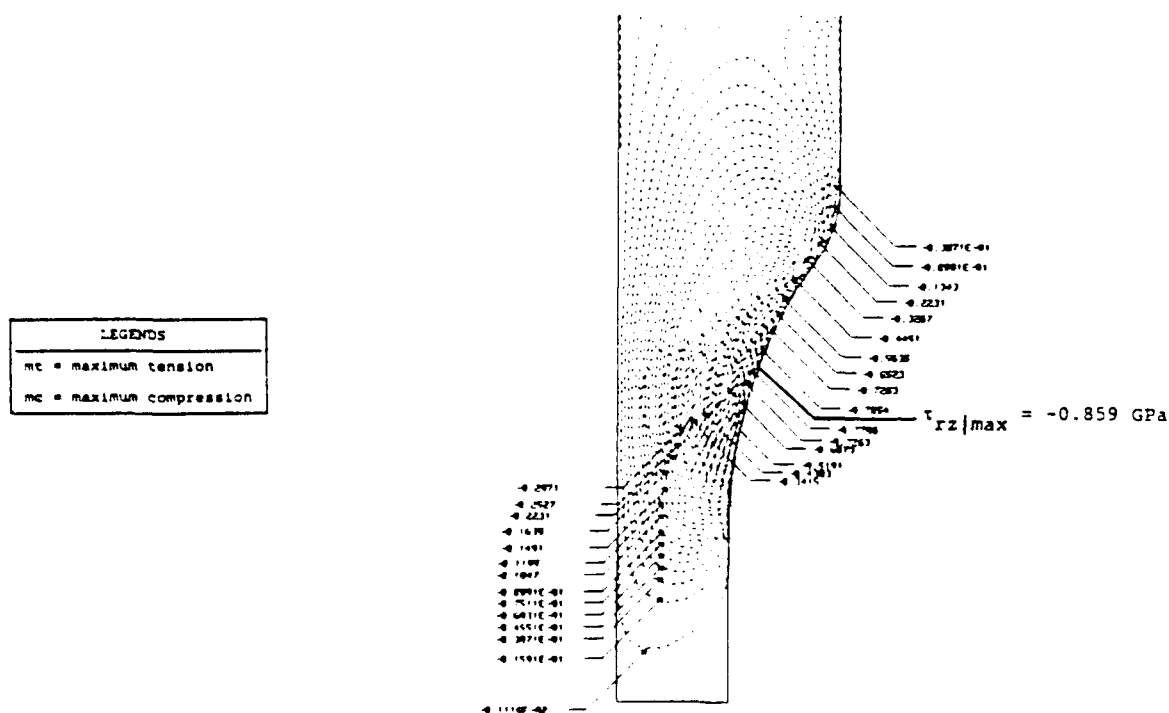


Figure 7d. Shear stress component ( $\tau_{rz}$ )  
(fine B-type model).

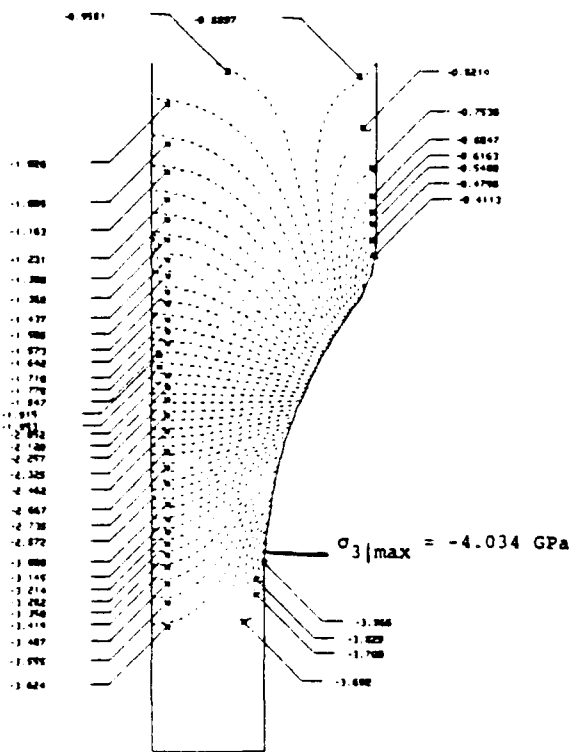
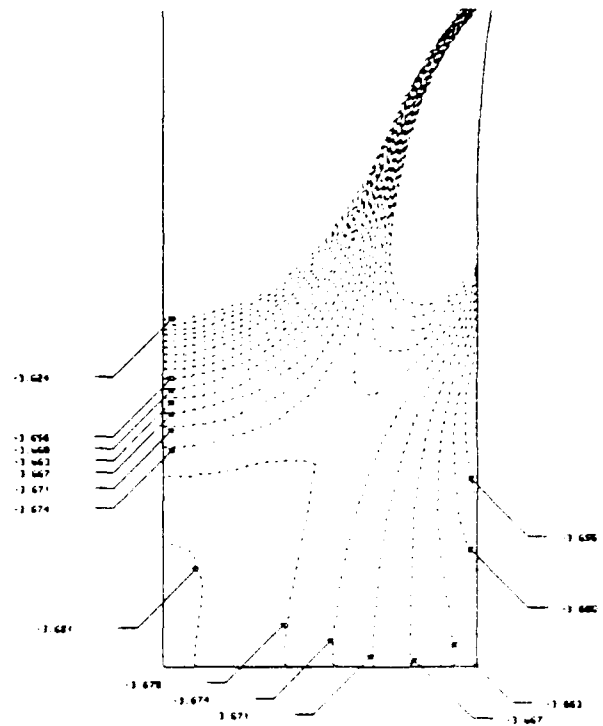


Figure 7e. 3rd principal stress ( $\sigma_3$ )  
(fine B-type model).



Gage Section Enlargement

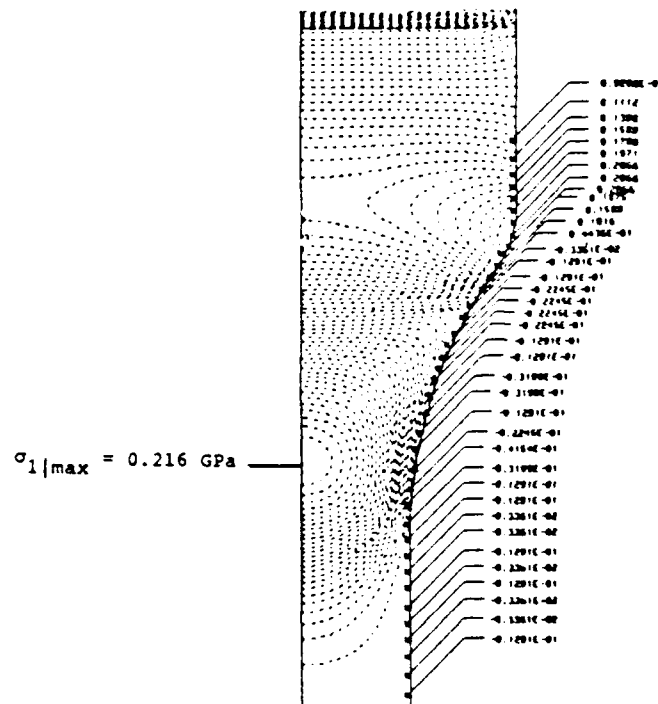
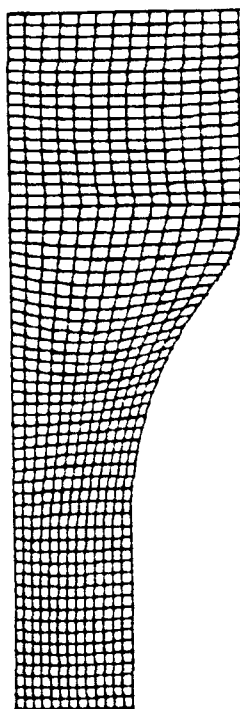
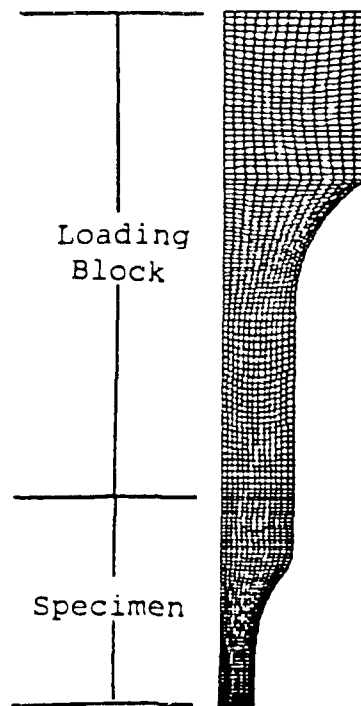
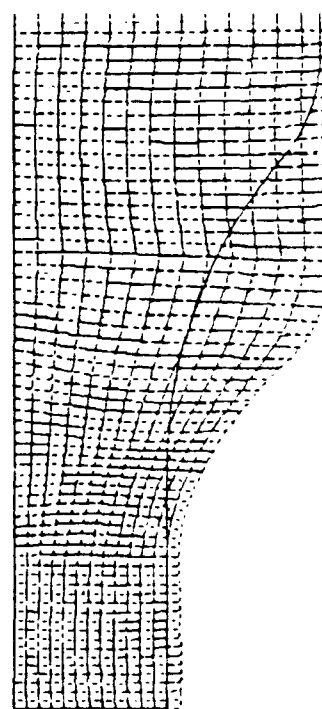


Figure 7f. 1st principal stress ( $\sigma_1$ )  
(fine B-type model).



Specimen



Deformed Model  
(Deformation is not to scale)

Figure 8. A-type fine model.



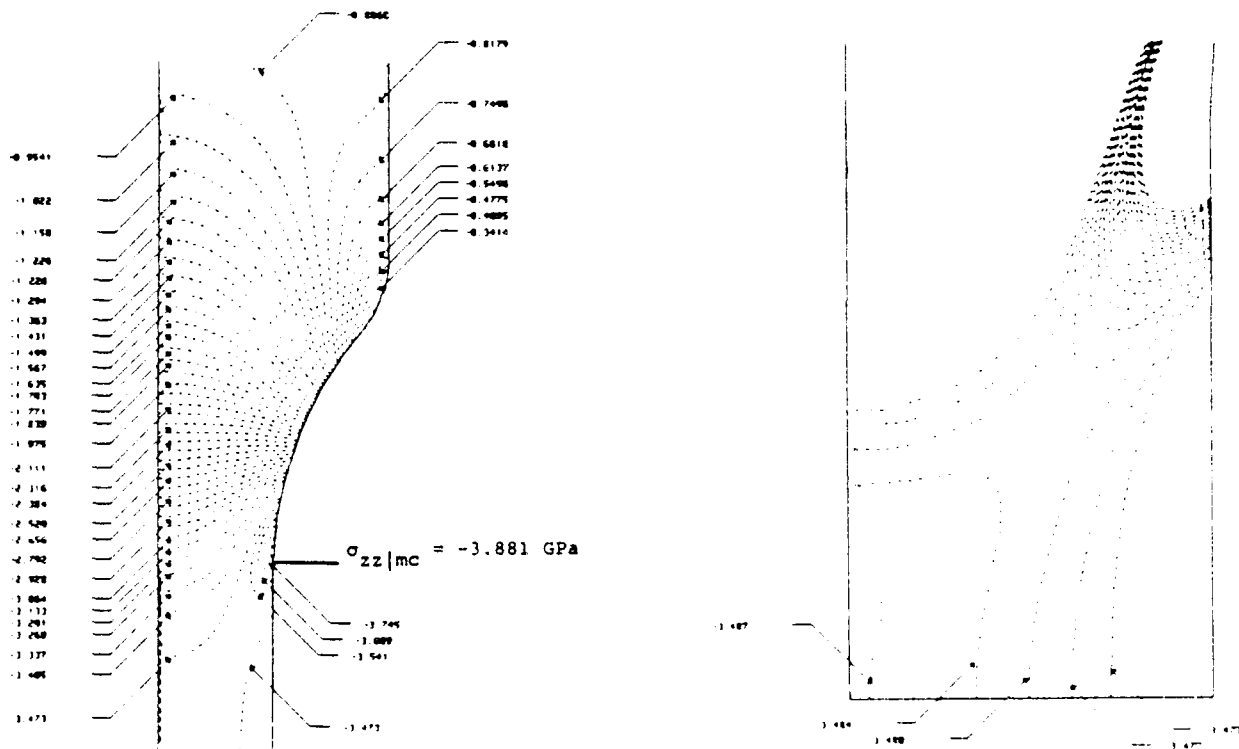


Figure 9a. Axial stress component ( $\sigma_{zz}$ )  
(fine A-type model).

Gage Section Enlargement

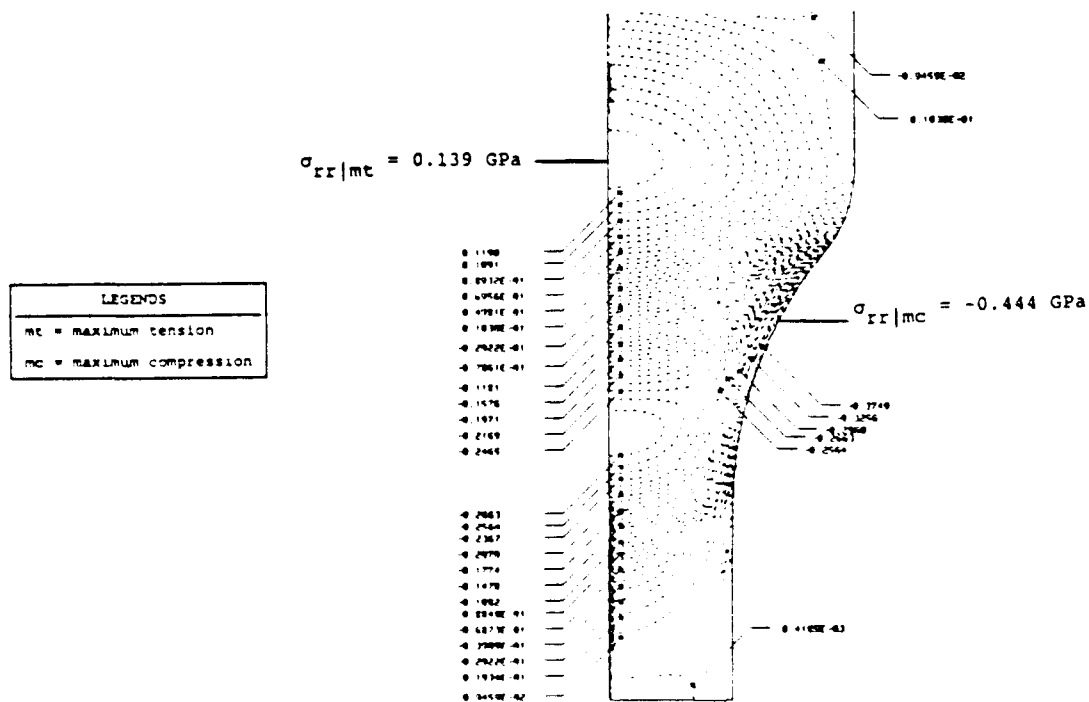


Figure 9b. Radial stress component ( $\sigma_{rr}$ )  
(fine A-type model).

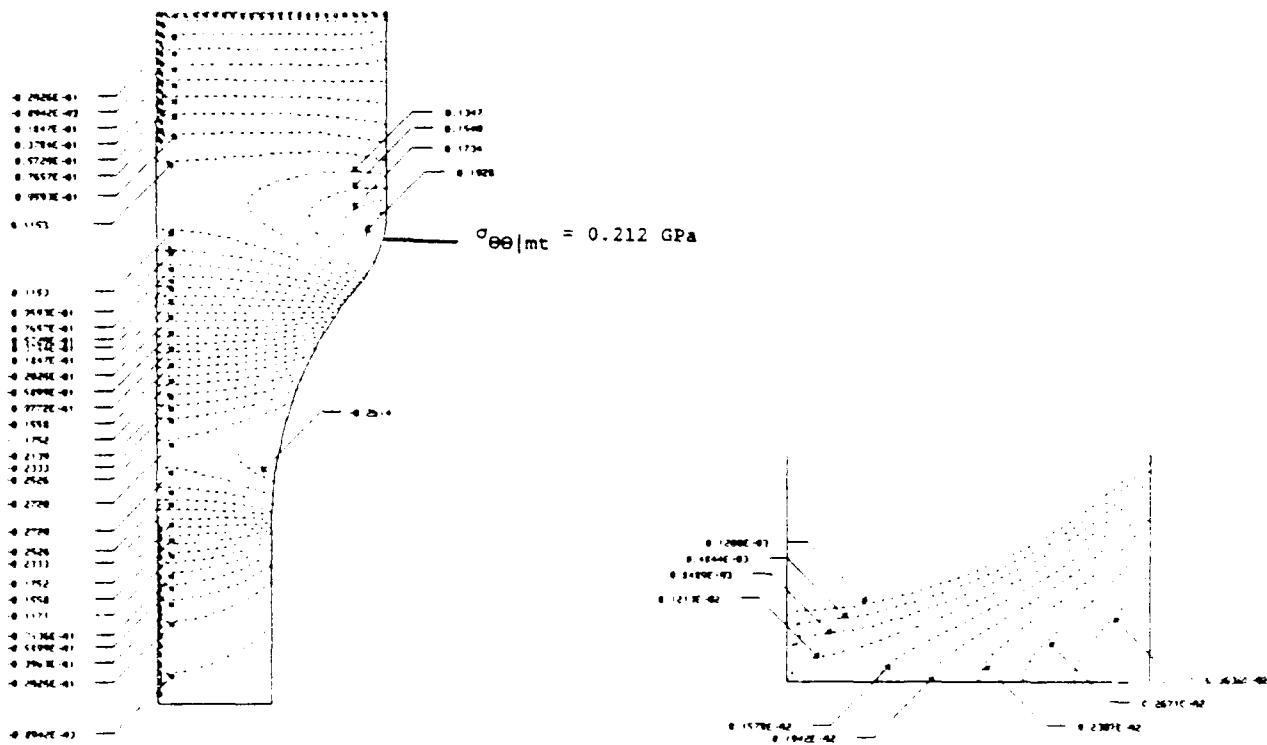


Figure 9c. Hoop stress component ( $\sigma_{\theta\theta}$ ) (fine A-type model).

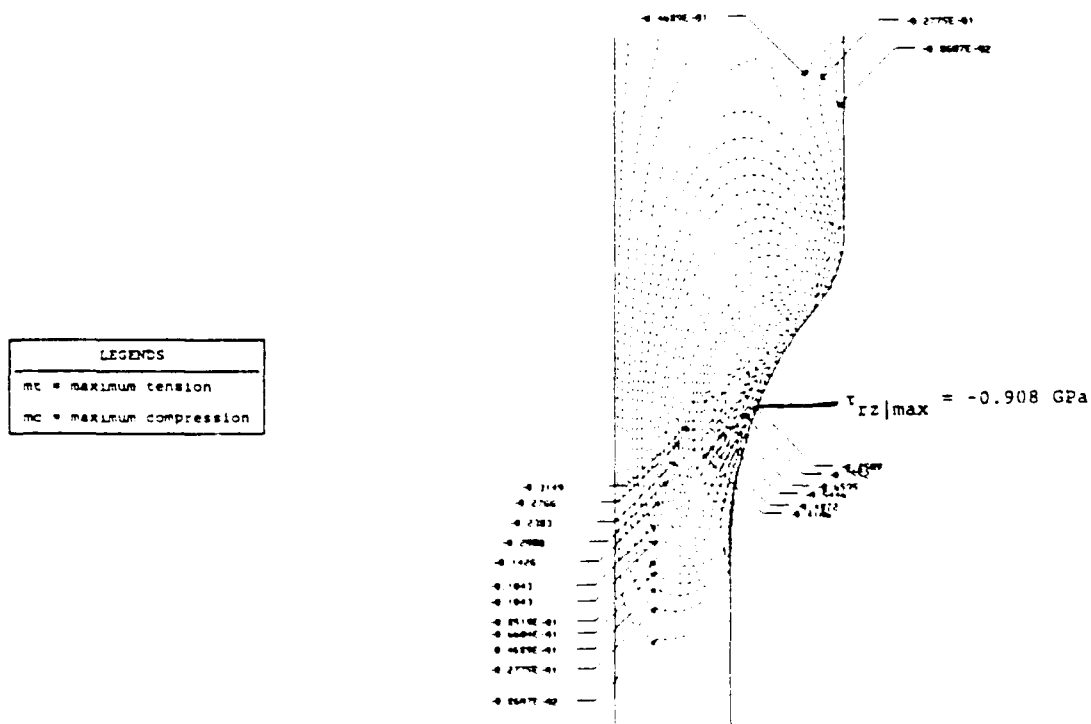


Figure 9d. Shear stress component ( $\tau_{rz}$ ) (fine A-type model).

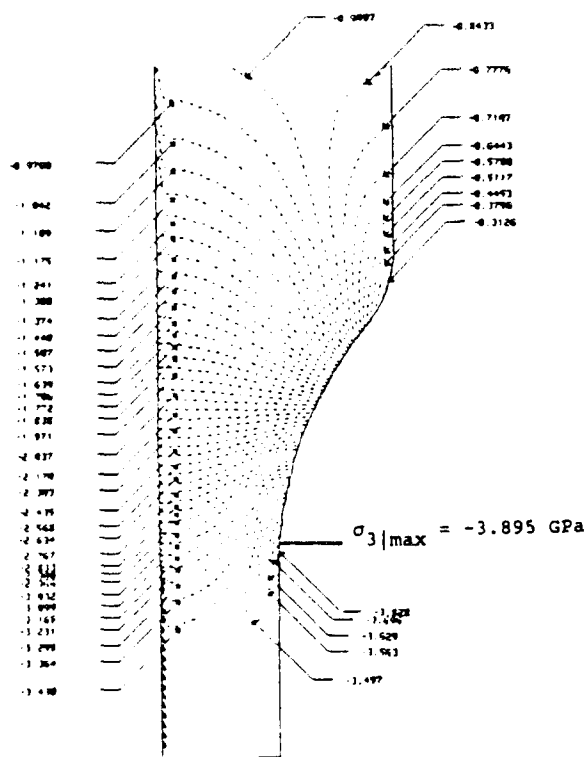
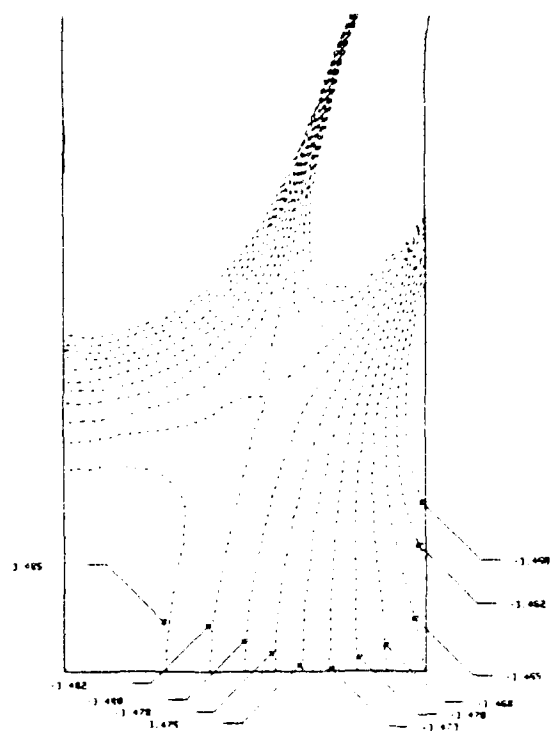


Figure 9e. 3rd principal stress ( $\sigma_3$ )  
(fine A-type model).



Gage Section Enlargement

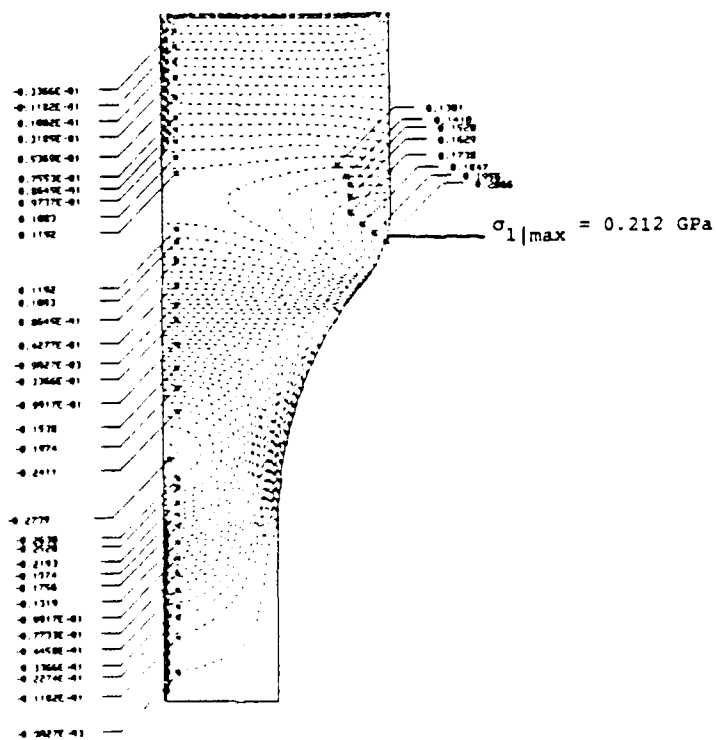


Figure 9f. 1st principal stress ( $\sigma_1$ )  
(fine A-type model).

# DISTRIBUTION LIST

No. of Copies	To
1	Office of the Under Secretary of Defense for Research and Engineering, The Pentagon, Washington, DC 20301
	Commander, U.S. Army Laboratory Command, 2800 Powder Mill Road, Adelphi, MD 20783-1145
1	ATTN: AMSLC-IM-TL
1	AMSLC-CT
	Commander, Defense Technical Information Center, Cameron Station, Building 5, 5010 Duke Street, Alexandria, VA 22304-6145
2	ATTN: DTIC-FDAC
1	MIAC/CINDAS, Purdue University, 2595 Yeager Road, West Lafayette, IN 47905
	Commander, Army Research Office, P.O. Box 12211, Research Triangle Park, NC 27709-2211
1	ATTN: Information Processing Office
	Commander, U.S. Army Materiel Command, 5001 Eisenhower Avenue, Alexandria, VA 22333
1	ATTN: AMCSCI
	Commander, U.S. Army Materiel Systems Analysis Activity, Aberdeen Proving Ground, MD 21005
1	ATTN: AMXS-YP, H. Cohen
	Commander, U.S. Army Missile Command, Redstone Scientific Information Center, Redstone Arsenal, AL 35898-5241
1	ATTN: AMSMI-RD-CS-R/Doc
1	AMSMI-RLM
	Commander, U.S. Army Armament, Munitions and Chemical Command, Dover, NJ 07801
1	ATTN: Technical Library
	Commander, U.S. Army Natick Research, Development and Engineering Center, Natick, MA 01760-5010
1	ATTN: Technical Library
	Commander, U.S. Army Satellite Communications Agency, Fort Monmouth, NJ 07703
1	ATTN: Technical Document Center
	Commander, U.S. Army Tank-Automotive Command, Warren, MI 48397-5000
1	ATTN: AMSTA-ZSK
1	AMSTA-TSL, Technical Library
	Commander, White Sands Missile Range, NM 88002
1	ATTN: STEWS-WS-VT
	President, Airborne, Electronics and Special Warfare Board, Fort Bragg, NC 28307
1	ATTN: Library
	Director, U.S. Army Ballistic Research Laboratory, Aberdeen Proving Ground, MD 21005
1	ATTN: SLCBR-TSB-S (STINFO)
	Commander, Dugway Proving Ground, Dugway, UT 84022
1	ATTN: Technical Library, Technical Information Division
	Commander, Harry Diamond Laboratories, 2800 Powder Mill Road, Adelphi, MD 20783
1	ATTN: Technical Information Office
	Director, Benet Weapons Laboratory, LCWSL, USA AMCCOM, Watervliet, NY 12189
1	ATTN: AMSMC-LCB-TL
1	AMSMC-LCB-R
1	AMSMC-LCB-RM
1	AMSMC-LCB-RP
	Commander, U.S. Army Foreign Science and Technology Center, 220 7th Street, N.E., Charlottesville, VA 22901-5396
3	ATTN: AIFRTC, Applied Technologies Branch, Gerald Schlesinger
1	Plastics Technical Evaluation Center, (PLASTEC), ARDEC, Bldg. 355N, Picatinny Arsenal, NJ 07806-5000
	Commander, U.S. Army Aeromedical Research Unit, P.O. Box 577, Fort Rucker, AL 36360
1	ATTN: Technical Library

No. of Copies	To
1	Commander, U.S. Army Aviation Systems Command, Aviation Research and Technology Activity, Aviation Applied Technology Directorate, Fort Eustis, VA 23604-5577 ATTN: SAVDL-E-MOS
1	U.S. Army Aviation Training Library, Fort Rucker, AL 36360 ATTN: Building 5906-5907
1	Commander, U.S. Army Agency for Aviation Safety, Fort Rucker, AL 36362 ATTN: Technical Library
1	Commander, USACDC Air Defense Agency, Fort Bliss, TX 79916 ATTN: Technical Library
1	Clarke Engineer School Library, 3202 Nebraska Ave. North, Ft. Leonard Wood, MO 65473-5000
1	Commander, U.S. Army Engineer Waterways Experiment Station, P. O. Box 631, Vicksburg, MS 39180 ATTN: Research Center Library
1	Commandant, U.S. Army Quartermaster School, Fort Lee, VA 23801 ATTN: Quartermaster School Library
1	Naval Research Laboratory, Washington, DC 20375 ATTN: Code 5830 Dr. G. R. Yoder - Code 6384
1	Chief of Naval Research, Arlington, VA 22217 ATTN: Code 471
1	Edward J. Morrissey, WRDC/MLTE, Wright-Patterson Air Force, Base, OH 45433-6523
1	Commander, U.S. Air Force Wright Research & Development Center, Wright-Patterson Air Force Base, OH 45433-6523 ATTN: WRDC/MLLP, M. Forney, Jr. WRDC/MLBC, Mr. Stanley Schulman
1	NASA - Marshall Space Flight Center, MSFC, AL 35812 ATTN: Mr. Paul Schuerer/EH01
1	U.S. Department of Commerce, National Institute of Standards and Technology, Gaithersburg, MD 20899 ATTN: Stephen M. Hsu, Chief, Ceramics Division, Institute for Materials Science and Engineering
1	Committee on Marine Structures, Marine Board, National Research Council, 2101 Constitution Ave., N.W., Washington, DC 20418
1	Librarian, Materials Sciences Corporation, 930 Harvest Drive, Suite 300, Blue Bell, PA 19422
1	The Charles Stark Draper Laboratory, 68 Albany Street, Cambridge, MA 02139
1	Wyman-Gordon Company, Worcester, MA 01601 ATTN: Technical Library
1	General Dynamics, Convair Aerospace Division, P.O. Box 748, Fort Worth, TX 76101 ATTN: Mfg. Engineering Technical Library
1	Department of the Army, Aerostructures Directorate, MS-266, U.S. Army Aviation R&T Activity - AVSCOM, Langley Research Center, Hampton, VA 23665-5225
1	NASA - Langley Research Center, Hampton, VA 23665-5225
1	U.S. Army Propulsion Directorate, NASA Lewis Research Center, 2100 Brookpark Road, Cleveland, OH 44135-3191
1	NASA - Lewis Research Center, 2100 Brookpark Road, Cleveland, OH 44135-3191
2	Director, U.S. Army Materials Technology Laboratory, Watertown, MA 02172-0001 ATTN: SLCMT-TML
1	Author

U.S. Army Materials Technology Laboratory  
Watertown, Massachusetts 02172-0001  
COMPARISON OF CERAMIC UNIAXIAL COMPRESSION  
SPECIMENS THROUGH DETAILED FINITE ELEMENT  
MODELLING -  
Paul V. Cavallaro

AD UNCLASSIFIED  
UNLIMITED DISTRIBUTION

Key Words

Ceramic materials  
Alumina  
Mechanical properties

Technical Report MTL TR 91-50, December 1991, 25 pp-  
illus-tables

Mechanical properties of advanced structural materials are determined through physical testing. In the area of high strength ceramics, routine testing includes techniques for measuring compressive strength. Successful and efficient characterization of compressive strength and other properties allows the design engineer to exploit the maximum structural potential for these advanced materials. This report details comparisons made between two proposed dumbbell-shaped, uniaxial ceramic compression specimens. Comparisons were made for alumina ( $Al_2O_3$ ) material through detailed finite element modeling. Differences in stress distributions resulting from both geometries were then applied to experimentally obtained strength values to determine if these values were representative of the same statistical population.

U.S. Army Materials Technology Laboratory  
Watertown, Massachusetts 02172-0001  
COMPARISON OF CERAMIC UNIAXIAL COMPRESSION  
SPECIMENS THROUGH DETAILED FINITE ELEMENT  
MODELLING -  
Paul V. Cavallaro

AD UNCLASSIFIED  
UNLIMITED DISTRIBUTION

Key Words

Ceramic materials  
Alumina  
Mechanical properties

Technical Report MTL TR 91-50, December 1991, 25 pp-  
illus-tables

Mechanical properties of advanced structural materials are determined through physical testing. In the area of high strength ceramics, routine testing includes techniques for measuring compressive strength. Successful and efficient characterization of compressive strength and other properties allows the design engineer to exploit the maximum structural potential for these advanced materials. This report details comparisons made between two proposed dumbbell-shaped, uniaxial ceramic compression specimens. Comparisons were made for alumina ( $Al_2O_3$ ) material through detailed finite element modeling. Differences in stress distributions resulting from both geometries were then applied to experimentally obtained strength values to determine if these values were representative of the same statistical population.

U.S. Army Materials Technology Laboratory  
Watertown, Massachusetts 02172-0001  
COMPARISON OF CERAMIC UNIAXIAL COMPRESSION  
SPECIMENS THROUGH DETAILED FINITE ELEMENT  
MODELLING -  
Paul V. Cavallaro

AD UNCLASSIFIED  
UNLIMITED DISTRIBUTION

Key Words

Ceramic materials  
Alumina  
Mechanical properties

Technical Report MTL TR 91-50, December 1991, 25 pp-  
illus-tables

Mechanical properties of advanced structural materials are determined through physical testing. In the area of high strength ceramics, routine testing includes techniques for measuring compressive strength. Successful and efficient characterization of compressive strength and other properties allows the design engineer to exploit the maximum structural potential for these advanced materials. This report details comparisons made between two proposed dumbbell-shaped, uniaxial ceramic compression specimens. Comparisons were made for alumina ( $Al_2O_3$ ) material through detailed finite element modeling. Differences in stress distributions resulting from both geometries were then applied to experimentally obtained strength values to determine if these values were representative of the same statistical population.

U.S. Army Materials Technology Laboratory  
Watertown, Massachusetts 02172-0001  
COMPARISON OF CERAMIC UNIAXIAL COMPRESSION  
SPECIMENS THROUGH DETAILED FINITE ELEMENT  
MODELLING -  
Paul V. Cavallaro

AD UNCLASSIFIED  
UNLIMITED DISTRIBUTION

Key Words

Ceramic materials  
Alumina  
Mechanical properties

Technical Report MTL TR 91-50, December 1991, 25 pp-  
illus-tables

Mechanical properties of advanced structural materials are determined through physical testing. In the area of high strength ceramics, routine testing includes techniques for measuring compressive strength. Successful and efficient characterization of compressive strength and other properties allows the design engineer to exploit the maximum structural potential for these advanced materials. This report details comparisons made between two proposed dumbbell-shaped, uniaxial ceramic compression specimens. Comparisons were made for alumina ( $Al_2O_3$ ) material through detailed finite element modeling. Differences in stress distributions resulting from both geometries were then applied to experimentally obtained strength values to determine if these values were representative of the same statistical population.